TEM Sample Preparation of Lithographically Patterned Permalloy Nanostructures on Silicon Nitride Membrane

Joshua Williams[1,2*], Michael I. Faley[1**], Joseph Vismal Vas[1], Penghan Lu[1], Rafal E. Dunin-Borkowski[1]

Address:

[1]Ernst Ruska-Centre for Microscopy and Spectroscopy with Electrons, Forschungszentrum Jülich, 52425 Jülich, Germany

[2]Faculty of Engineering, University Duisburg-Essen, 47057 Duisburg, Germany

* Email: j.williams@fz-juelich.de

** Email: m.faley@fz-juelich.de

Abstract

We have prepared ferromagnetic (FM) nanostructures intended for the investigation of high-frequency magnetization dynamics in permalloy (Py) nanodisks using Lorentz transmission electron microscopy (LTEM). Py nanodisks were fabricated on thin silicon nitride (SiN) membranes using three different fabrication methods: lift-off, ion beam etching (IBE), and stencil lithography and analyzed using different instruments: scanning electron microscope (SEM), LTEM, and electron holography. A bilayer of positive PMMA resist was utilized in the first method to form an undercut structure that guarantees a clean lift-off procedure. The second approach used dry etching with an Ar beam to etch a thin Py film, while an electron-beam-patterned negative resist mask

kept the desired structure. In the third process, nanostencils (shadow masks) with submicron apertures were milled on SiN membranes using focused ion beam. Furthermore, we have developed a new TEM sample preparation method, where we fabricated Py nanostructures on a bulk substrate with a SiN buffer layer and etched the substrate to create a thin SiN membrane under the Py nanostructures. Finally, we observed a vortex magnetization of the Py nanodisk using LTEM and off-axis electron holography. A correlation between preparation methods and the properties of the Py nanostructures was observed.

Keywords

Permalloy; nanodisk; nanofabrication; magnetic imaging; Lorentz transmission electron microscopy, electron holography;

Introduction

The ability to study magnetization dynamics of ferromagnetic nanostructure is important for developing nanoelectronics, particularly for data storage and information processing. A vortex spin configuration has been observed on Py nanodisks [1-2] and the feature that is appealing about magnetic vortex is its independence between polarity and helicity [3]. Since then, many studies have been done on manipulating magnetic vortex inside Py nanodisk from simulation [4-6] to examining under magnetic force microscope [7], under electron microscope [1, 8-11], as well as under magneto-optical kerr effect microscope [12-13]. Possible applications of Py nanodisk were proposed for zero hysteresis magnet sensors, magnet logic, and data storage [14]. Py is a nickel-iron alloy (80at% Ni and 20at% Fe) that has a small coercive field (H_c) [15]

and low magnetostriction (λ_s) [16] as well as high permeability and high saturation magnetization (M_s) [17].

Transmission electron microscopy (TEM) offers a high spatial resolution for magnetic imaging. This allows correlative characterization to investigate magnetic information down to the nanoscale and simultaneously obtain the structural and chemical information of the material. However, the corresponding samples need to be prepared on electron beam transparent membranes which are very fragile and can easily break during standard lithography procedures. Although a lift-off approach has been demonstrated [18], alternative methods may be advantageous in terms of structural resolution, process simplicity, and the absence of resist residues [19]. We have fabricated ferromagnetic nanodisks on a conventional TEM grid from TedPella® using three different fabrication methods.

In the first method, a bilayer of positive PMMA resist created an undercut structure. The resist was patterned using electron beam, which offers higher resolution compared to other sources e.g. UV light, because of the small electron source and smaller wavelength of electrons in comparison to UV light . Since the use of ultrasonic bath will destroy the free-standing membrane, the undercut must be deliberately made larger to ensure a clean lift-off process. An approach to create a larger undercut is realized by multi-dose exposure, which consists of two parts: The main exposure to pattern the nominal structure and an additional exposure to pattern the outline of the nominal structure. This additional exposure is performed with a lower dose than the main exposure so that it does not induce chain scission on the top resist layer, but only the bottom resist more sensitive layer. The result of the multi-dose exposure was controlled by observing a cross-section of the developed bilayer resist using a SEM in snapshot mode to avoid melting of PMMA resist. The second approach involved etching a thin Py film with an ion beam while preserving the intended structure with an electron-

beam-patterned negative resist mask. Redeposition of etched material was found to construct fences at the edges of the structures. Fences and edge roughness from the imperfect lift-off process were reported to influence the magnetic properties of nanostructures [21]. The third method, stencil lithography, makes use of a shadow mask, which was fabricated by milling submicron apertures on an identical conventional TEM grid using focused ion beam. This method avoids the use of resist-based fabrication, which is common in preparing nanodisk samples for TEM [8, 18].

In addition, we have developed a method of sample preparation for patterned nanostructures starting with a bulk substrate. This method is versatile and might be useful for more complicated lithographically patterned nanostructures to be examined by using TEM. The results of the fabrication methods mentioned above were examined by using SEM. This is important because the structural information (disk dimensions and deformation from fences) later correlates to the magnetic properties. A vortex spin configuration only happens under the right diameter-thickness ratio, otherwise either a single or multiple magnetic domains will appear.

At last, we did TEM experiments by using magnetic imaging techniques such as Lorentz transmission electron microscopy (LTEM) and off-axis electron holography. LTEM takes advantage of the Lorentz force

$$F = -e\,(v \times B), \tag{1}$$

as the electron beam is deflected by the circular oriented magnetic fields inside a sample in a vortex state of magnetization. Fresnel imaging captures a defocused image so that inwardly deflected electron beams overlap (white contrast) and outwardly deflected beams leave an empty area (black contrast) [22].

Off-axis electron holography is done by interfering with the primary signal from the magnetic sample with a reference wave and the intensity result is as follows:

$$I_{hol}(r) = |\Psi_i(r) + \exp[2\pi i\, q\cdot r]|^2 = 1 + A_i^2(r) + 2A_i(r)\cos[2\pi i\, q\cdot r + \varphi_i(r)]. \tag{2}$$

Notice that the phase from the electron wave as a function of plane coordinate $\varphi_i(r)$ contributes to the third term inside the cosine, and this can be retrieved by taking the Fourier transform (FFT) of the intensity [23]. The divergence of the phase shift is proportional to the in-plane magnetic field inside the sample.

Fabrication Processes and Results

1. Fabrication on Commercial SiN Membrane

1.1. Lift-off

The lift-off procedure is described in Figure 1. We use PMMA and its copolymer as a positive resist to create a bilayer resist. The copolymer (AR-P 617.08) is a methyl methacrylate and methacrylic acid copolymer dissolved in 1-methoxy-2-propanol with a solid content of 8 percent. The viscosity is 36 mPas and as it is spun at 4000 rpm and baked at 200° C for 25 minutes, it has a thickness of around 500 nm. To spincoat a 3 mm TEM grid (Figure 2a and 2b), we used a special adapter (Figure 2c). The high baking temperature and relatively long baking duration were chosen because the copolymer must be solid to prevent dissolution by the PMMA layer. In addition, the baking temperature can control the copolymer's sensitivity. The higher the baking temperature of the copolymer, the more sensitive the copolymer gets because more intensive anhydrides form a 6-ring form of methacrylic acid, the form breaks apart easier than the aliphatic chain remainder during electron beam exposure [24]. AR-P 679.04 is polymethylmethacrylate (PMMA) dissolved in ethyl lactate with a solid content of 4 percent. The molecular weight is 950 K and has a high resolution respectively low sensitivity. The viscosity is 16.4 mPas and as it is spun at 4000 rpm and baked at 180°C for 5 minutes, it has a thickness of around 300 nm. The exposure

is done by the electron beam machine Vistec EBPG 5000+ operating at 100 kV. Working on a thin transparent membrane also allows a high-resolution patterning, since there is less electron scattering during exposure [25].

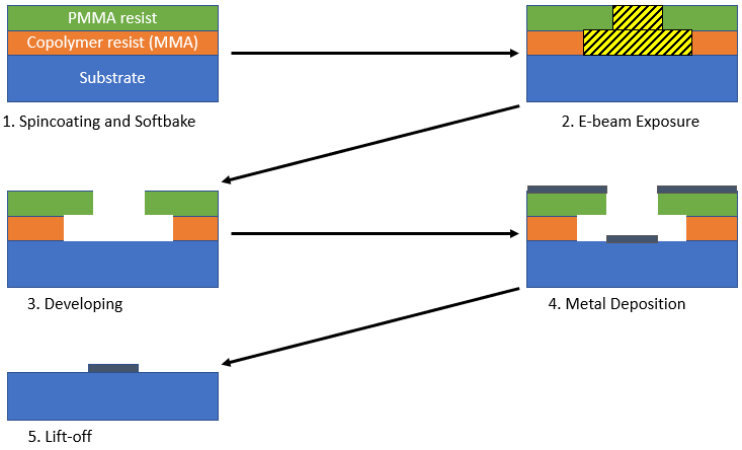

Figure 1: “Lift-off” fabrication process.

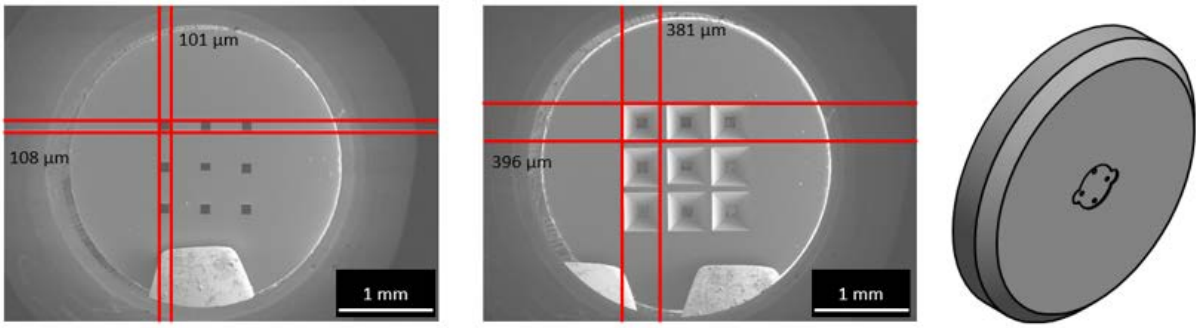

a) b) c)

Figure 2: a) SEM images of the front side. b) backside (right) of 3 mm TEM window grid, which provides 9 windows of free-standing 50 nm thick SiN membrane. c) spin coating adapter for 3 mm TEM grid.

The purpose of applying two layers of resist is to create a large undercut, by choosing a more sensitive bottom layer than the top. This prevents the unwanted deposition of metal that sticks to the side of the resist after lift-off. A larger undercut was achieved on multilayer resist with the help of multiple exposures [26]. The idea is to expose the resist layer by layer: The bottom resist was deposited and exposed and then aluminum

was deposited as a spacer between the bottom and top layer, to prevent the top layer from dissolving the lower one. Next, the top resist layer was deposited and exposed in the nominal sizes. The structure was developed from top to bottom including removal of Al spacer. The development of the bottom layer in other words the size of the undercut is controlled only by the development time. In a more recent study, the Al spacer was omitted, and the development was done with one solution since the bilayer resist is made from PMMA and its copolymer [27]. The process is quite time-consuming since the exposures were done layer by layer.

Considering the two technologies, a one-time exposure is possible with the help of high accelerating voltage during electron beam exposure. In this process, rather than doing one resist deposition and exposure after another, the layer selectivity is controlled by the electron beam dose and the sensitivity of the two layers. Only copolymer (higher sensitivity) carried out the chain scission reaction at low doses, and at higher doses, both layers were exposed. The exposure scheme is given as follows:

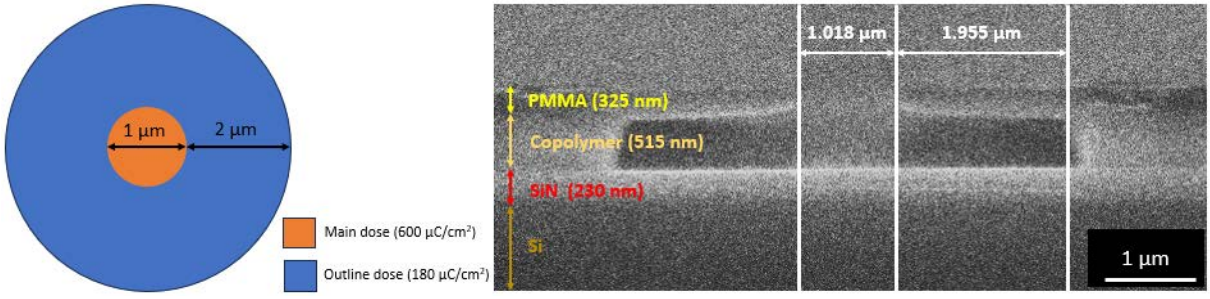

a) b)

Figure 3: a) Electron beam exposure scheme. b) Cross-section (right) of developed resist with multi-dose exposure on a bulk substrate taken by SEM in snapshot mode.

The doses are chosen by considering that the copolymer is 2 – 3 times more sensitive than the PMMA [24]. If the exposure dose is too small, then the undercut will not develop, but if it is too high, then the PMMA will dissolve bigger than the nominal diameter.

Once the resist is developed, we deposit a 50 nm thick of Py using magnetron sputtering through the resist aperture. We used DC magnetron sputtering in a pure Ar environment at a pressure of 1 Pa to deposit thin films of Py at room temperature. The effective permalloy target had a diameter of 8 mm. The sputtered material almost resembles a parallel beam when it approaches the substrate at a target-substrate distance of around 8 cm. The sputtered film was investigated under HR-TEM and it was revealed that the film is polycrystalline with a lattice spacing of 0.36 nm (Figure 4), which correlates to the lattice constant of Py.

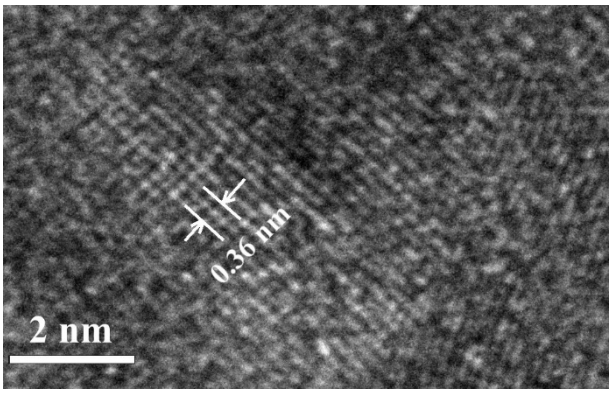

Figure 4: HR-TEM image of Py nanodisk. The grain sizes are around 6 nm.

The "lift-off" technique allows the fabrication down to a 400 nm disk array spaced 200 nm apart. With the help of the undercut, there is significantly less debris of metal after lift-off (Figure 5a). In comparison, the arrows on the lower part of Figure 5d demonstrate the lift-off result without a big undercut that leads to fences from the Py deposited on the sides of the resist. There are, however, a few limitations to consider: The spincoated resist may be inhomogeneous (edge bead) on smaller substrate, reducing the region where high-quality structures may be obtained. Furthermore, one cannot deposit metal in high temperature and one has to establish a good thermal contact during metal deposition to prevent the resist mask from moving as the

substrate temperature is above the glass transition temperature of the resist.

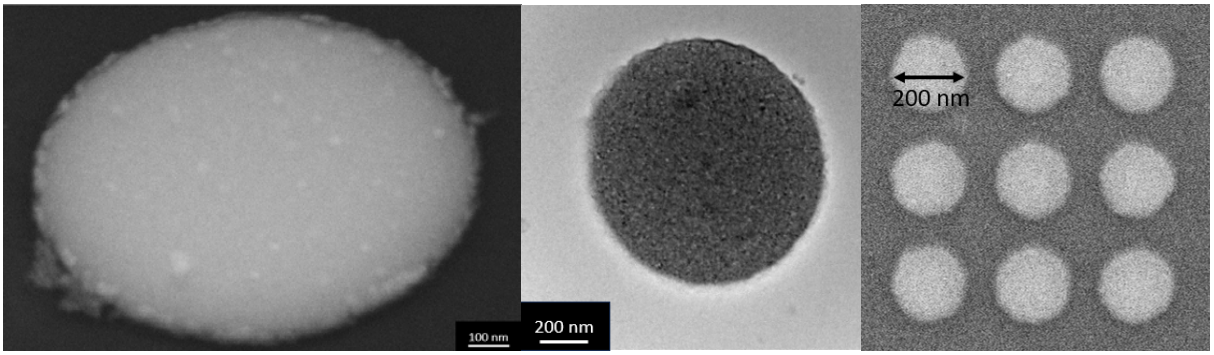

a) b) c)

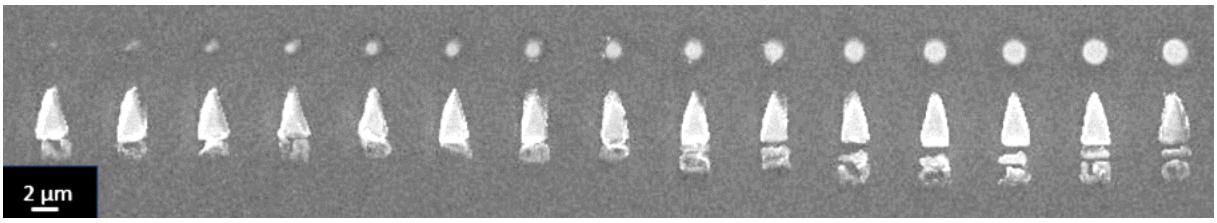

d)

Figure 5: a) SEM image of 1 µm Py disk with 50 nm thick at a tilt angle. b) TEM image of 1 µm Py disk. c) SEM image of 200 nm array with 50 nm spacing. d) SEM image of Py nanodisks of different sizes.

1.2 Ion Beam Etching

The IBE process (Figure 6) is as follows: The first step is to deposit Py on the substrate and then spincoat a negative resist on top. The resist used is AZ® nLof 2020 diluted with AZ® EBR solvent. The producers describe this as a photoresist (UV) but it is also compatible with electron beam. It is spun on top of Py at 4000 rpm and baked at 110° Celsius for 1 minute. The resulting thickness is around 448 nm for a 1:1 diluted resist and around 203 nm for a 1:2 diluted resist. The resist is exposed to 120 µC/cm^2 at 100 kV and then post exposure bake at 110°C for 2 minutes. The development is done by emerging the sample in AZ® 726MIF containing 2.38% Tetramethylammonium hydroxide (TMAH) for 20 seconds.

Once the resist is developed, IBE is performed. Since the ions diverge as it travels, the substrate is rotated to have a uniform ion flux on the substrate and a uniform etching rate between the inner and outer side. The highest etching rate can be achieved when the substrate is tilted at 45° since the etching rate of the primary beam is much bigger than the redeposition rate of etched materials. As observed in Figure 7, there was redeposition of etched material along the edge of the resist. This can be avoided by taking an additional step before etching the Py: The resist is heated at 120°C for 5 minutes to reflow the resist and creating a meniscus shape thus decreasing the redeposition on the side of resist during etching.

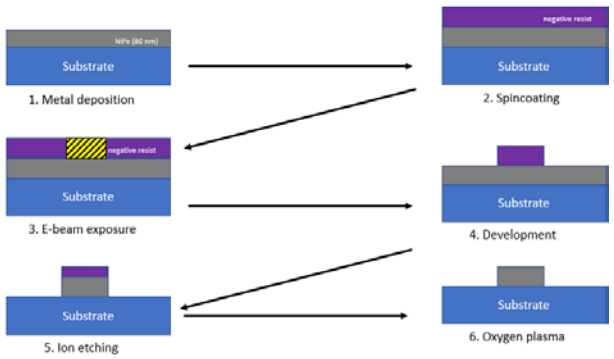

Figure 6: Ion beam etching fabrication process

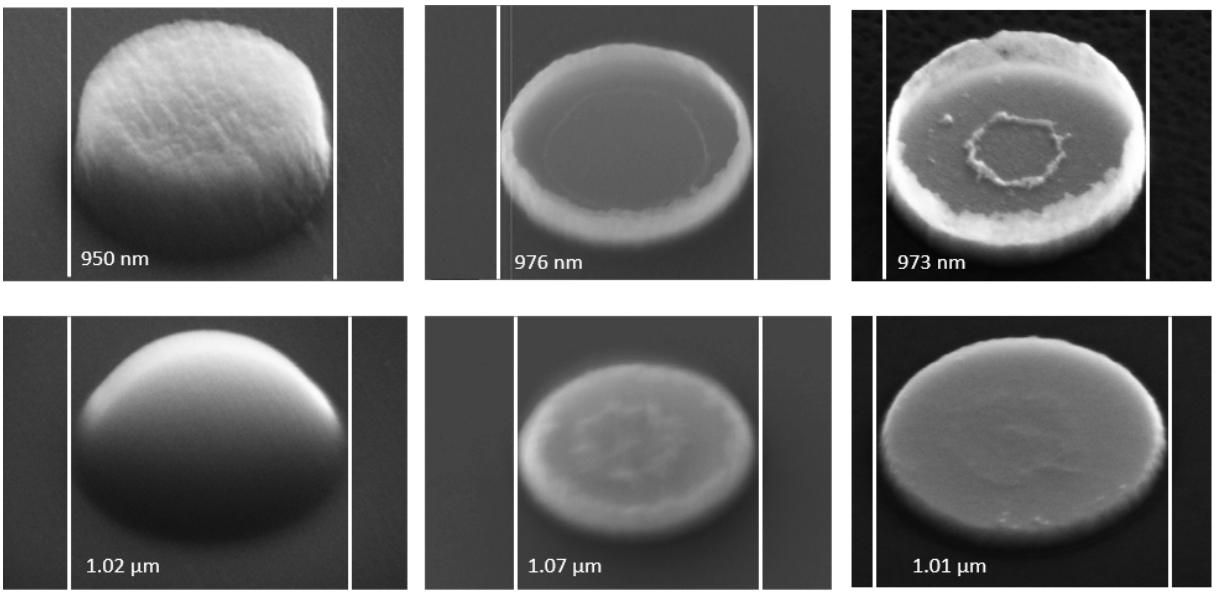

Figure 7: Comparison between normal patterned resist (top) and reflow resist (bottom). From left to right: Patterned resist, nanodisk after IBE, and nanodisk after plasma cleaning.

The advantage of IBE is the well-defined structures with good edge sharpness (Figure 8). This technique offers high resolution structure down to 200 nm and dense structures with spacing as small as 50 nm can be created. Another advantage is the ability to deposit metal at high temperatures, as the resist mask is applied after the metal deposition. However, there are also some drawbacks to consider. The sample is physically etched by Argon bombardment, which results in a non-selective etching of the material. Non-selective etching means not only Py is etched but also the resist and the SiN membrane. Areas around the nanodisks are thicker and rougher due to the lower etch rate near the structures and the redeposition of permalloy. In addition, the much thinner areas of the membrane away from the nanostructures can affect the overall mechanical stability of the membrane. Dry etching is generally better suited for bulk substrate applications discussed in subchapter 2.

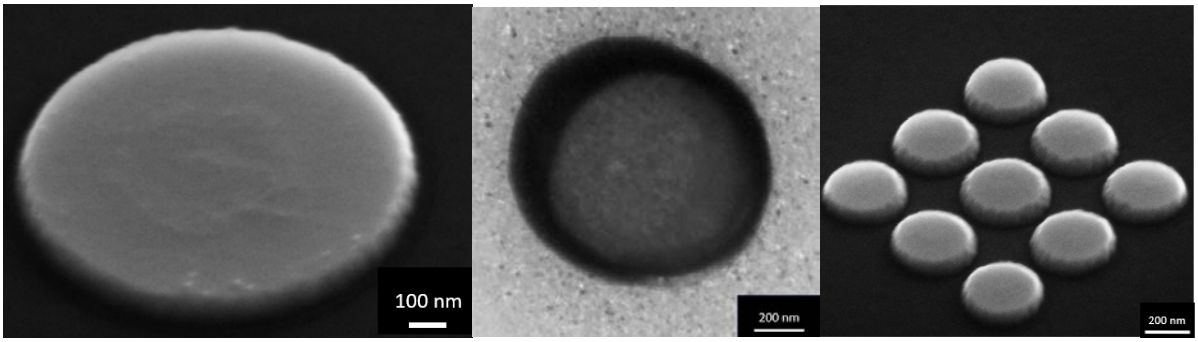

a) b) c)

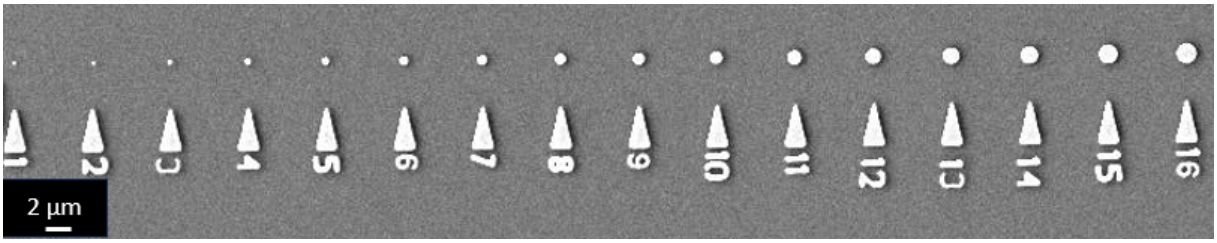

d)

Figure 8: a) SEM image of 1 µm Py disk with 80 nm thick at a tilt angle b) TEM image of 1 µm Py disk. c) SEM image of 200 nm array with 50 nm spacing. d) SEM Images of nanodisk with different sizes.

1.3 Stencil lithography

Stencil lithography was implemented back in 1978 to fabricate thin film Josephson devices [28]. The principle behind stencil lithography is to deposit materials onto the substrate through the aperture of the hard mask. Rather than placing the mask directly on the substrate and then removing it, as in traditional resist-based fabrication, stencil lithography employs a separate mask that is later aligned on the substrate and retains its aperture after the pattern transfer. This technique has the advantages including the method's simplicity, reusable masks, and the absence of resist masks, which eliminates common challenges associated with resist such as edge bead problem and resist melting during deposition. This approach is ideal for applications on small substrates where spincoating a homogeneous resist layer is difficult. This technique is particularly suitable for our application because our TEM substrate has the SiN membrane required for the mask.

The mask fabrication process (Figure 9a) is the following: A conventional TEM grid with a free-standing silicon nitride membrane was deposited 200 nm thick of aluminium by means of evaporation. The aluminium layer serves as a support for the free-standing membrane and as a conductive layer for better imaging during FIB milling. Then FIB milling was performed to create apertures on the silicon nitride membrane representing the patterns to be transferred to the sample. Lastly, the aluminium layer was removed by emerging the mask on TMAH 3% solution. In this project, a TEM substrate with 9 free-standing SiN membranes was used as a hard mask. We lay an identical substrate flat on the mask on a flip chip configuration. The mask is aligned so

that all 9 windows are on top of each other and the asymmetrically broken windows serve as an orientation aid. The substrate and mask were fixed using Kapton® foil with adhesive layer. After deposition, the foil can be removed and the mask can be detached. The mask can still be used, but the resulting nanodots will be smaller than those obtained from the previous deposition because the aperture size on the mask is reduced by residual deposited material.

As seen in Figure 9c, the structure has a blurring effect. One of the sources of blurring in stencil lithography is the geometry of the source-stencil-substrate configuration. The deposited structure is larger than the stencil aperture and their size difference (the blurring size) is proportional to the size of the source and the distance between the substrate and the mask, and inversely proportional to the sample-to-source distance [29]. It is then required to decrease the distance between the mask and the substrate as well as to employ an evaporation process from a distant point-like source. Furthermore, metal deposits on the mask apertures lead to clogging, causing masks to become ineffective after multiple uses.

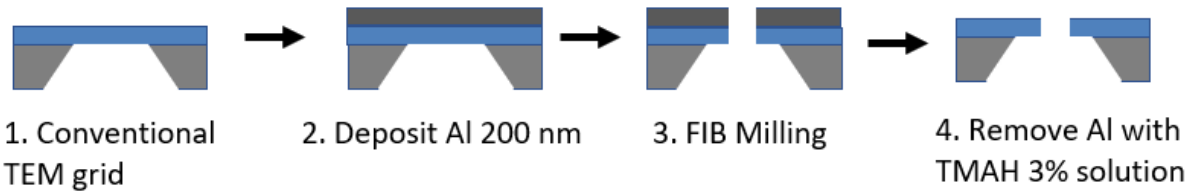

a)

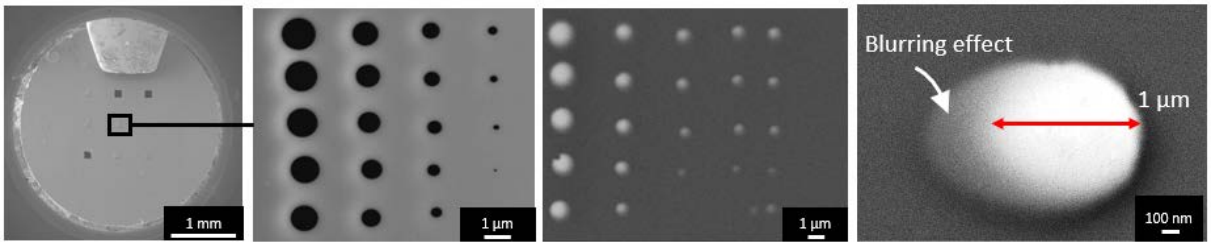

b) *c)*

Figure 9: a) Hard mask preparation. b) SEM image of the hard mask c) SEM image of the deposited Py and 1 µm disk.

2. Sample preparation of nanostructure starting on bulk substrate

To avoid the delicate procedure of fabricating nanostructures on a freestanding SiN membrane, we initially fabricated the nanostructures on a 200 µm thick Si substrate with a 100 nm thick SiN buffer layer on both sides. The buffer layers were deposited with low-pressure CVD to ensure a stress-free film. The fabrication process is as follows:

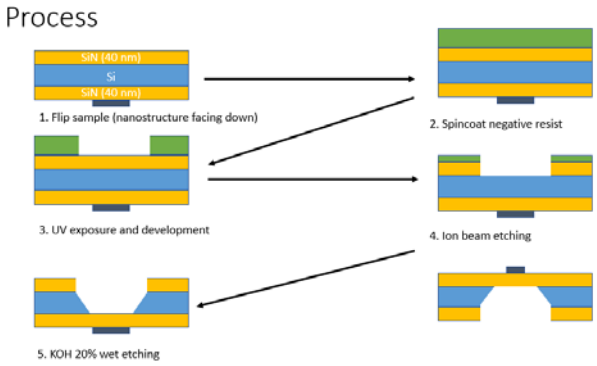

Figure 10: SiN membrane preparation on a nanostructure

First, we made the nanostructure using the lift-off or IBE method on the bulk substrate, then we protected the nanostructure with a resist and patterned AZ®5214E resist on the back side of the substrate using the image reversal technique. A window in the SiN buffer layer was prepared by ion beam etching through the aperture in the mask of AZ®5214E resist and the remaining SiN layer served as a hard mask for the wet etching of the substrate backside in 20% KOH solution. The KOH solution was heated to 60°C to accelerate the process to an etching rate of approximately 9 µm/h in the direction perpendicular to the substrate surface. Using a warmer KOH resulted in a faster etch rate but leaded to a much stronger bubbling and roughening of Si surface with creation of micropyramidal hillocks [30].

The surface alignment of the Si substrates is parallel to the {100} crystallographic plane of Si and because of the KOH anisotropic etching results to 54.7° slope with respect to etched surface on the sidewalls. Due to the (010) edge orientation of Si substrates, etching occurs faster in diagonal directions of the substrates, resulting in sharp edges on the structure (Figure 11b).

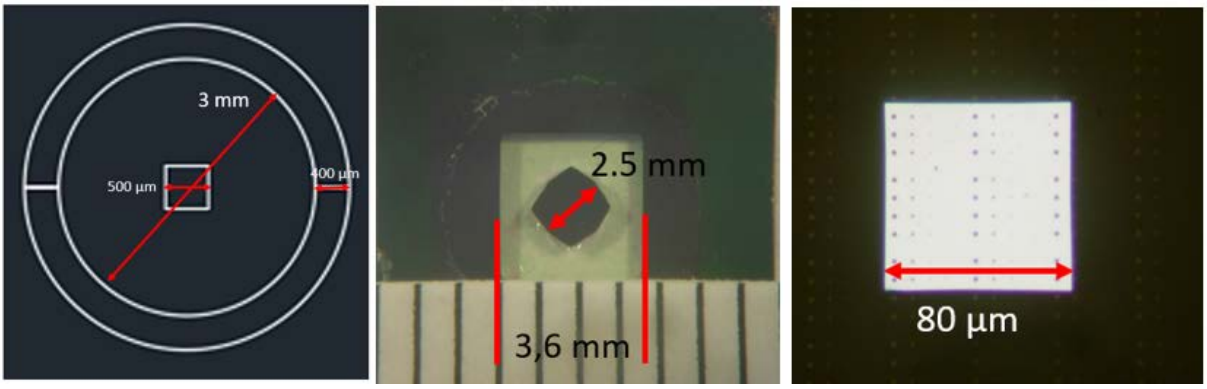

a) b) c)

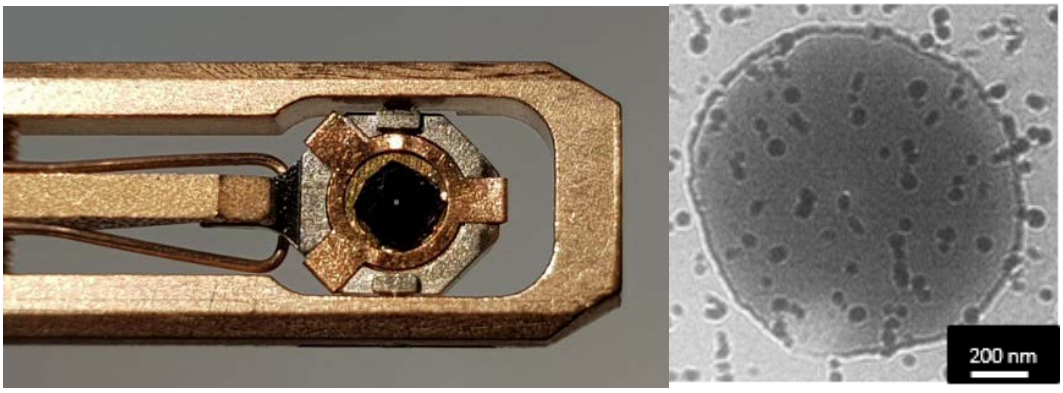

d) e)

Figure 11: a) Lithography mask. b) The etched substrate is still attached to the bulk substrate. c) Freestanding SiN membrane. d) TEM substrate glued on a 3 mm ring is mounted on the TEM holder. e) LTEM image of 1 µm Py disk on SiN membrane. The small dots are residuals of the protective resist layer.

Experiments

Setup

During LTEM, the objective lens is usually turned off so that the magnetic information of the sample is not distorted by the lens, and a smaller dedicated objective lens for LTEM is used instead. The normal objective lens was turned on in our setup, and the magnetic field was generated in the same direction as the electron beam to initialize the magnetic state of the sample and induce an external magnetic field on the sample. By tilting the sample, an in-plane (H_{ip}) and out-of-plane (H_{oop}) field is applied to the sample (Figure 12). We kept the tilt angle constant and applied different intensities of the objective lens respectively external magnetic field and observed the magnetization of the sample under LTEM and off-axis electron holography.

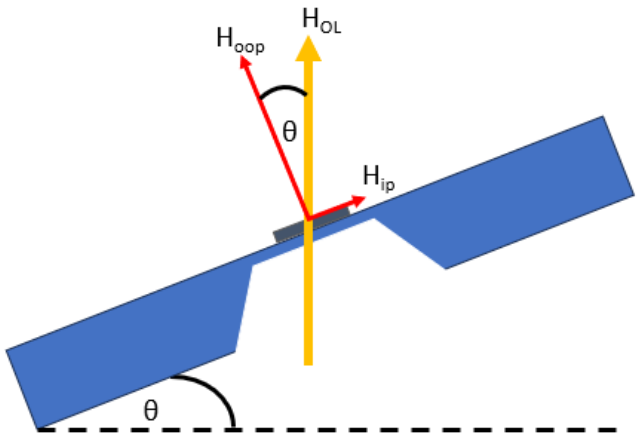

Figure 12: Tilted sample and the external magnetic field component

Lorentz TEM

When electrons interact with a magnetic field, they encounter a Lorentz force, which causes them to be deflected. The electron beam is deflected by magnetic field that are perpendicular to the electron beam, in this case in-plane magnetic components on the sample. Lorentz TEM exploits this phenomenon with two different approaches:

Foucault imaging deploys a lens to capture the deflected electron beam and Fresnel imaging captures a defocused picture which gives bright contrast as the deflected electrons converge to a region or dark contrast as the deflected electrons diverge.

As we captured an overfocused image of a magnetic vortex, a counterclockwise helicity deflected the electron beam inward, resulting in a bright spot at the vortex core, whereas clockwise helicity results in a dark spot (Figure 13). The contrast can be changed from dark to bright, and vice versa, by inverting the defocus.

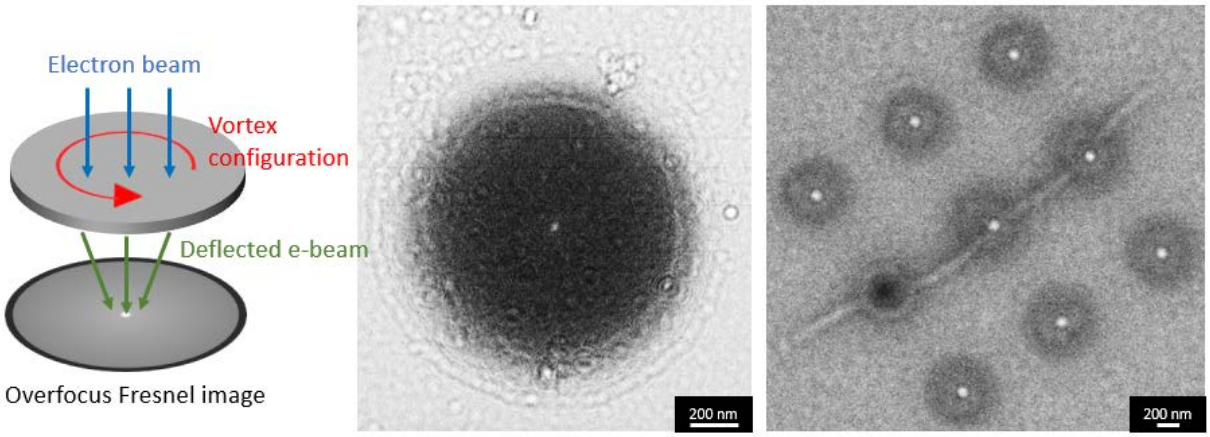

a) b) c)

Figure 13: a) simplified illustration of LTEM technique b) LTEM image of 1µm disk c) LTEM image of 400 nm disk array.

As explained in the setup, we induced the external field on the sample up until the contrast was no longer visible, which means we saturated the magnetic component until all pointed to the same in-plane direction. Afterward, we decreased the external field to observe the vortex after saturation and increased the field in the opposite direction. Lastly, we decreased the field to zero. The LTEM observation of Py disk under external field is given in the complementary part.

As external magnetic field is applied, the vortex core (bright or dark spot) moves perpendicular to the applied field toward the edge of the disk where the magnetization

component opposes the applied field as the area where the magnetization component is aligned with the field grows bigger. The vortex core displacement is in linear proportion to the applied magnetic field as calculated [31]. At the saturation field, the vortex core disappears because the magnetization is now in single domain. All the moments point in the same direction of the field, so that the electrons are deflected in the same direction and no convergence or divergence of electron beam can be captured.

As the external magnetic field was decreased, the nucleation of the vortex does not happen instantly but after the field reaches around 30 mT then bright spot appears near the edge of the disks. The same thing happened as we applied the opposite field direction until saturation and start decreasing it. This is consistent with the result provided before [32].

Off-axis Electron Holography

The limitation of LTEM is that the magnetic contrast only exists when there is a different orientation between magnetic domains inside the sample. Using off-axis electron holography, we were able to directly examine the in-plane magnetization direction. Using the same parameter as the LTEM experiment, we kept the tilt angle of the sample constant and started with increasing the external field from 0 Oe up to 530 Oe (Figure 14 upper row), which is bigger than the saturation field we observed during LTEM experiment. Then, we decreased the magnetic field back to 0 Oe (Figure 14 bottom row). We observed the movement of vortex core parallel to the applied field and the vortex state under external field of 335 Oe before and after saturation are different, since the nucleation starts right after the external field decreased to 300 Oe. The results are consistent with the observation under LTEM.

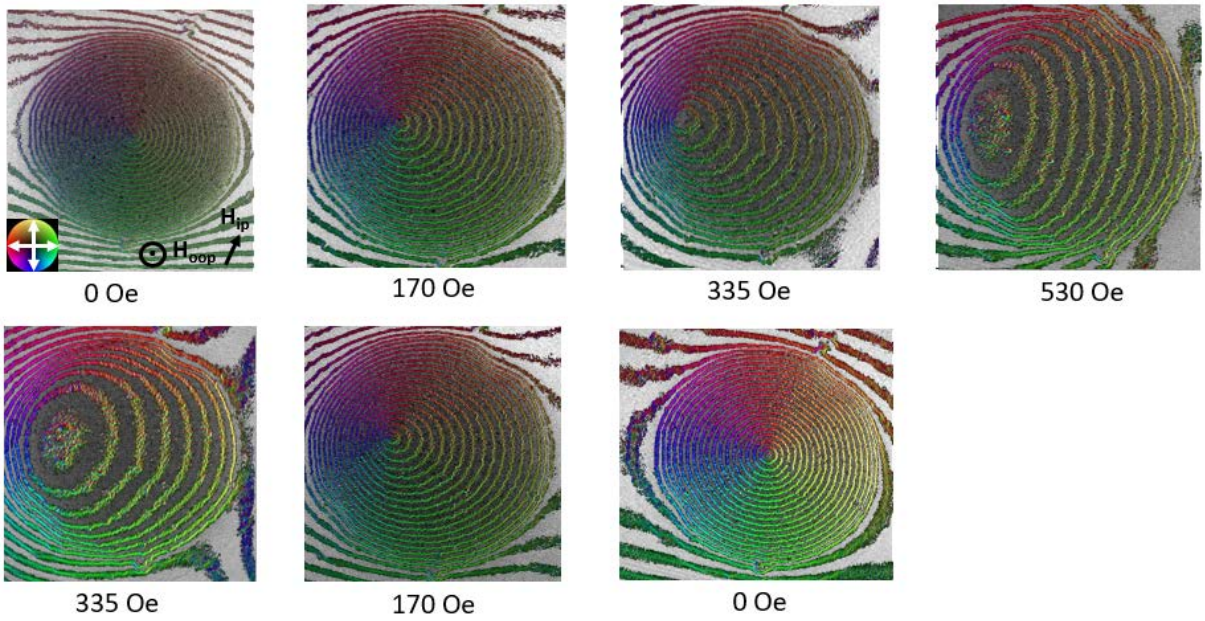

Figure 14: Off-axis electron holography of nanodisk under various magnetic fields. Fringes outside of the disk are probably caused by the charging of the SiN membrane.

Conclusion

Electron beam lithography in combination with “lift-off” and IBE methods for the preparation of Py nanodisks has been optimized. Their results have been compared through SEM, LTEM, and electron holography. In addition, the application of stencil lithography for the preparation of Py nanodisks has been demonstrated and the results are compared with the results obtained with the electron beam lithography.

Among these methods, dry etching stands out for its sharp and well-defined edges, while the hard mask method offers the least precise results. In a broader comparison, ion beam etching (IBE) outperforms the "Lift-off" technique, delivering cleaner and more reproducible nanostructures with better spatial resolution. "Lift-off" fabrication allows for the creation of nanodisks with dimensions ranging from 400 nm to 1.6 µm, but as the size decreases, structural precision diminishes. On the other hand, dry etching can achieve nanodisks as small as 200 nm with high precision. However, it is

important to consider that the IBE process may result in thinner structural membranes, potentially compromising their mechanical stability. Furthermore, IBE, which is a physical etching process, redeposited a non-volatile metal layer on the resist creating fences on the edge of the structure and contaminating the silicon nitride membrane. A possible solution is replacing IBE with RIE, then there will be less redeposition since the reaction between gas and etched metal will form a gaseous compound or volatile particles that can be pumped out by the vacuum. RIE of Nickel-Iron alloy has been done by using induced coupled plasma RIE with argon and chlorine gasses [33] or with NH_3 and CO gasses [34]. Stencil lithography requires further optimization although the possible applications are attractive due to the flexibility of the patterns, reusable masks, and resistless fabrication. This would be suitable because TEM grids are too small for standard lithography. After all, the spincoated resist has on TEM grids inhomogeneous thickness due to the presence of the edge beads that become too large relative to the diameter of the TEM grid. Alignment of the stencil mask in a flip-chip configuration with the sample in clean room conditions prior to metal deposition plays an important role as a single dust particle can increase the gap between the mask and the sample up to a 100-fold scale, thereby increasing the shadowing effect greatly.

The KOH etching method opens further applications for TEM sample preparation for more complicated high-resolution nanostructures. We have developed a straightforward method to prepare SiN membrane while having nanostructure on one side. This method allows the use of ultrasonic bath, higher deposition temperatures, and homogeneous resist layer, all of which are difficult to obtain with free-standing SiN membranes, resulting in more reproducible results. In principle, some characterizations that do not require an electron beam transparent membrane can be done while the nanostructures are on a bulk substrate. Once all measurements have been completed, KOH etching can be conducted, and as a result, the sample is placed

on a free-standing SiN membrane and can be studied under TEM. This is useful for future high-frequency correlative characterization of multilayer spintronic devices. Another possible further development is to use a different membrane for example SiC (silicon carbide, lattice constant 0.435 nm) since it can grow as a single crystalline layer and ensure an epitaxial growth of sample on top of it, such as NbN (a = 0.439 nm) with lattice mismatch of 1%. Epitaxial growth of Py films on single-crystal SiC membranes is also feasible: Py epitaxial films were obtained on single-crystal MgO substrates [35] that have a lattice constant of 0.42 nm. It was demonstrated that the epitaxial SiC layer can serve as an excellent mask material for KOH etching of Si [36]. However, etching down to a crystalline membrane might be different than etching to a freestanding amorphous SiN membrane. The structural integrity of freestanding crystalline membrane during KOH etching is still to be investigated. An alternative to KOH etching would be FIB Milling as demonstrated by Mayr et. al. [37].

Our observation of magnetic vortex behavior under external magnetic field is consistent with other publications.

Supporting Information

Lorentz TEM Video

File Format: .mp4

Acknowledgments

The authors gratefully acknowledge the possibility of performing parts of the work at ER-C-1, HNF, PGI-4/JCNS-2, PGI-5, and PGI-7 in Forschungszentrum Jülich GmbH. The authors also thank R. Borowski, L. Kibkalo, L. Risters, S. Neduev, M. Nonn, H.

Stumpf, S. Trellenkamp, F. Lentz, E. Neumann, O. Petracic, S. Nandi, B. Schmitz and G. Potemkin for technical assistance.

Funding

This research was funded in parts by the EU Horizon 2020 Research and Innovation Programme (Grant No. 856538, project “3D MAGiC”) and the Joint Laboratory on Model and Data Driven Material Characterization of the Helmholtz Association.

References

1. Raabe, J.; Pulwey, R.; Sattler, R.; Schweinböck, T.; Zweck, J.; Weiss, D. *Journal of Applied Physics* **2000**, 88.7, 4437-4439.

2. Shinjo, T.; Okuno, T.; Hassdorf, R.; Shigeto, K.; Ono, T. *Science* **2000,** 289, 930–932.

3. Pulwey, R.; Rahm, M.; Biberger, J.; Weiss, D. *IEEE Transactions on Magnetics* **2001**, 37, no. 4, 2076-2078.

4. Liu, Y.; Gliga, S.; Hertel, R.; Schneider, C.M. *Applied Physics Letter* **2007**, 91, 11.

5. Pang, Z.; Yin, F.; Fang, S.; Zheng, W.; Han, S. *Journal of Magnetism and Magnetic Materials* **2012**, 324, 5, 884-888.

6. Xu, M.; Jiang, G.; Zhang, Z.; Li, R.; Meng, D.; Zhang, J. *Journal of Physics D: Appl. Phys.* **2022,** 55, 325303.

7. Okuno, T.; Shigeto, K.; Ono, T.; Mibu, K.;Shinjo, T. *Journal of Magnetism and Magnetic Materials* **2002**, 240, 1-6,

8. Schneider, M.; Hoffmann, H.; Zwick, J. *Appl. Phys. Let.* **2000**, 77, 2909–2911.

9. Harvey, T.R.; Rubiano da Silva, N.; Gaida, J.H. MRS Bulletin **2021,** 46, 711–719.

10. Weßels T. ; Däster, S.; Murooka, Y.; Zingsem, B.; Migunov, V.; Kruth, M.; Finizio, S.; Lu, P.; Kovács, A.; Oelsner, A.; Müller-Caspary K.; Acremann, Y.; Dunin-Borkowski R.E. *Ultramicroscopy* **2022**, 233, 113392.

11. Fu, X.; Pollard, S.D.; Chen, B.; Yoo, B.; Yang, H.; Zhu, Y. *Science* Advances. **2018**, 4.

12. Dieterle, G.; Gangwar,A.; Gräfe, J.; Noske,M.; Förster, J.; Woltersdorf, G.; Stoll,H.; Back,C.H.; Schütz, G. *Appl. Phys. Let.* **2016**, 108, 022401.

13. Mehrnia, M.; Trimble, J.; Heinonen, O.; Berezovsky, J. *Physical Review Applied*, **2016**, 16, 034049.

14. Cowburn, R. *Journal of Magnetism and Magnetic Materials* **2002**, 242–245, 505–511.

15. Lloyd, J.C.; Smith, R. S. *Journal of Applied Physics* **1959**, 30.

16. McKeehan L.W.; Cioffi, P.P.; *Phys. Rev*. **1926**, 28, 146-157.

17. Arnold, H.D.; Elmen, G. W. *Journal of the Franklin Institute* **1923**, 195, 621-632.

18. Dhankhar M.; Vaňatka M.; Urbanek M. *Journal Vis. Exp*. **2018,** 137, 57817

19. Faley, M.I.; Williams, J.; Lu, P.; Dunin-Borkowski, R.E. *Electronics* **2023**, 12, 2144.

21. Bryan, M.T.; Atkinson, D.; Cowburn, R. P. Journal of Physics **2005**, 85, 40–44.

22. Reeve, R. M.; Elmers, H. J.; Büttner, F.; Kläui, M. Magnetic Imaging and Microscopy. In. M. Coey, S. Parkin (eds.), Handbook of Magnetism and Magnetic Materials, Springer Nature Switzerland AG **2021**, 1-52.

23. Kovács, A.; Dunin-Borkowski, R. E. Handbook of Magnetic Material. Magnetic imaging of nanostructures using off-axis electron holography; Brück, E.; Elsevier: Amsterdam, Netherlands, 2018; pp. 59–153.

24. https://www.allresist.com/wp-content/uploads/sites/2/2020/03/AR-P610_english_Allresist_product-information.pdf. (accessed August 24th 2023)

25. Edelstein, A.S. Nanomaterials : Synthesis, Properties and Applications, Inst. of Physics Publ.: Bristol, U.K., 2001.

26. Dolan, G.J. *Applied Physics Letters* **1977**, 31, 337–339.

27. Bogdanov, A.L.; Andersson, E. K. *SPIE Proceedings* **1991**.

28. Dunkleberger, L.N. *Journal of Vacuum Science and Technology* **1978**, 15, 88–90.

29. Vazquez-Mena, O. ; Villanueva, L. G. ; Savu, V. ; Sidler, K. ; Langlet, P.; Brugger, J. *Nanotechnology* **2009**, 20, 415303.

30. Schröder, H.; E Obermeier, E.; Steckenborn, A. *J. Micromech. Microeng*. **1999**, 9 139

31. Guslienko, K. Y.; Novosad, V.; Otani, Y.; Shima, H.; Fukamichi, K. *Phys. Rev. B* **2001**, 65, 024414.

32. Uhlig, T.; Rahm, M.; Dietrich, C.; Höllinger, R.; Heumann, M.; Weiss, D.; Zweck, J. *Phys. Rev. Let.* **2005**, 95, 237205.

33. Park, H.J.; Ra, H. W.; Song, K. S.; Hahn, Y. B. *Korean Journal of Chemical Engineering* **2004**, 21, 1235–1239.

34. Kim, S.D.; Lee, J. J.; Lim, S. H.; Kim, H. J. *Journal of the Magnetics Society of Japan* **1999**, 23, 252–254.

35. Ohtake, M.; Tanaka, T.; Matsubara, K.; Kirino, F.; Futamoto, M. *Journal of Physics: Conference Series* **2011,** 303, 012015.

36. Mohd Nasir, N.F.; Shah, C.M.; Leech, P.W.; Reeves, G.K.; Pirogova, E.; Istivan, T.; Tanner, P.; Holland, A.S. Fabrication of 3C-Silicon Carbide Membranes: Towards Development of Novel Microdevices for Biomedical Applications. 2012 International Conference on Biomedical Engineering (ICoBE),27-28 February 2012, Penang.

37. Mayr, S.; Finizio, S.; Reuteler, J.; Stutz, S.; Dubs, C.; Weigand, M.; Hrabec, A.; Raabe, J.; Wintz, S. *Crystals* **2021**, 11, 546.